

Three-Dimensional Numerical Simulation of Ni-YSZ Anode Polarization Using Reconstructed Microstructure from FIB-SEM Images

K. Matsuzaki, D. Kanno, H. Teshima, N. Shikazono and N. Kasagi

Department of Mechanical Engineering, The University of Tokyo, Hongo 7-3-1,
Bunkyo-ku, Tokyo 113-8656, Japan

The overpotential in a three-dimensional Ni-YSZ anode model structure obtained by a dual-beam focused ion beam-scanning electron microscope is predicted by lattice Boltzmann method. Gaseous, ionic and electronic transport equations with electrochemical reaction at the three-phase boundary are solved with an assumption of local equilibrium in the solid oxide. The gas transport is modeled by a so-called dusty gas model. The numerical simulation is performed under the current density conditions of 0.01, 0.1, 0.3 and 0.7 A/cm². Three-dimensional electrochemical potential distributions inside a test anode microstructure are presented. The proposed method can be used for predicting SOFC electrode polarization.

Introduction

Solid oxide fuel cells (SOFCs) are a most powerful candidate for the future energy systems, because of their high efficiency and fuel flexibility (1). Anode porous microstructures are known to have significant effects upon the cell performance and durability of SOFCs. However, the quantitative relationship between the anode microstructure and the polarization resistances has not been fully investigated. Recently, direct measurements of three-dimensional SOFC electrode microstructures have been reported using focused ion beam scanning electron microscopy (FIB-SEM) (2-5) and X-ray computed tomography (XCT) (6). In addition to these experimental approaches, a numerical simulation tool for predicting electrode performance in actual microstructures is strongly demanded.

In the present study, actual anode three-dimensional microstructure obtained by a dual-beam focused ion beam-scanning electron microscopy (FIB-SEM) (7) is used for numerical simulation. The anode overpotential is calculated by the lattice Boltzmann method (LBM) (8), and the predicted overpotential is compared with the experimental data (9) for validation. Furthermore, the three-dimensional distribution of oxygen ion electrochemical potential is presented.

Reconstructed Microstructure

An electrolyte supported button cell is used in the present study (9). The Ni-8YSZ ratio is 50:50 vol.%. Cross-sectional images (26 nm/pixel) are obtained at a 62 nm interval by a dual-beam focused ion beam-scanning electron microscopy (FIB-SEM, Carl Zeiss NVision 40) (7). The volume size is 18.60 × 8.43 × 6.20 μm³. Pore, Ni and YSZ phases are distinguished by their brightness values. Then, three-dimensional microstructure is re-meshed to 62 nm cubic voxels for the numerical analysis.

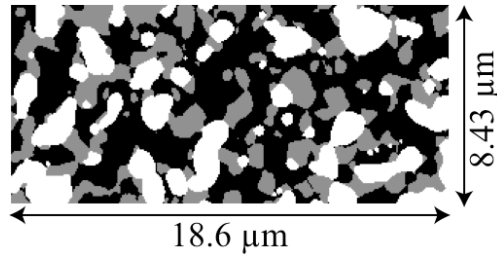


Figure 1. Phase distinguished microscopy image, white: Ni, gray: YSZ, black: pore.

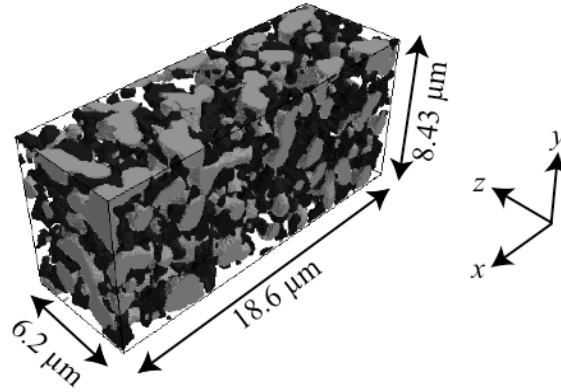


Figure 2. Reconstructed Ni-YSZ anode microstructure, gray: Ni, black: YSZ.

Figure 1 shows an example of the phase distinguished cross-sectional image, while the reconstructed three-dimensional microstructure is shown in Figure 2.

Numerical Method

Computational Domain

For securing a sufficiently large electrode thickness, five mirrored FIB-SEM structures is repeated in the z direction. The electrolyte is located at $z = 0 \mu\text{m}$, and the current collector (CC) is assumed at $z = 31 \mu\text{m}$. Thicknesses of electrolyte and CC layers are $1.302 \mu\text{m}$ and $0.62 \mu\text{m}$, respectively. The resultant computational domain is represented in Figure 3.

Governing Equations

Gaseous, electronic and ionic diffusion equations are solved inside each of the obtained three-dimensional Ni, YSZ and pore phases. In the gaseous phase, hydrogen and steam diffusion is solved based on a dusty gas model (DGM) (10). When constant total pressure is assumed, DGM is written as follows:

$$\frac{N_i}{D_{i,k}} + \sum_{j \neq i} \frac{y_j N_i - y_i N_j}{D_{i,j}} = -\frac{1}{RT} \nabla p_i, \quad [1]$$

where y_i is the molar fraction and N_i is the molar flux. Subscripts i and j present gas species, such as hydrogen and steam. Graham's law is led from Eq. [1] as:

$$\sum_i N_i \sqrt{M_i} = 0. \quad [2]$$

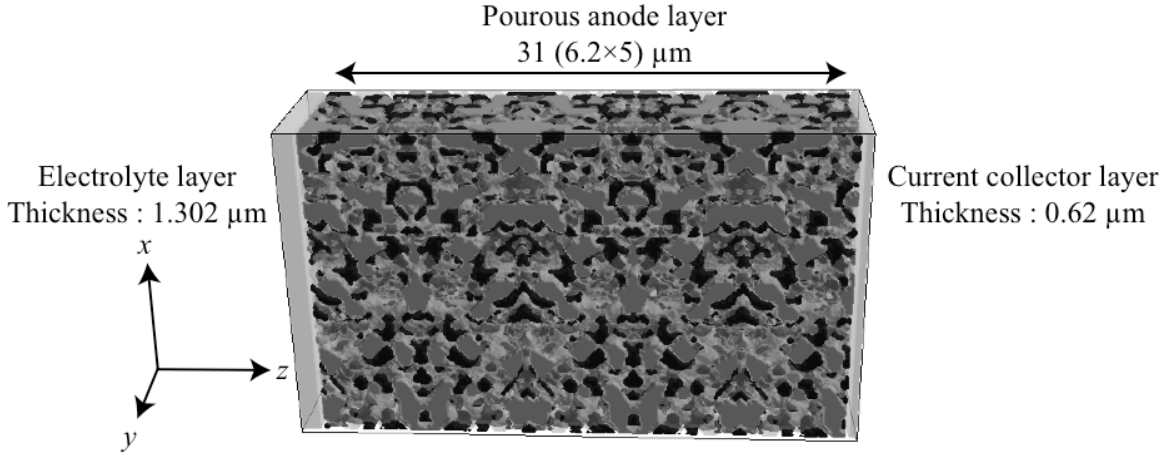


Figure 3. Schematic of computational domain, gray: Ni, black: YSZ.

Therefore, the diffusion equation of hydrogen is expressed as:

$$\nabla \left(\left[\frac{1 - \alpha y_{\text{H}_2}}{D_{\text{H}_2, \text{H}_2\text{O}}} + \frac{1}{D_{\text{H}_2, \text{k}}} \right]^{-1} \nabla C_{\text{H}_2} \right) = \frac{i_{\text{react}}}{2F}, \quad [3]$$

where C_{H_2} is the molar concentration of hydrogen gas, and

$$\alpha = 1 - \left(\frac{M_{\text{H}_2}}{M_{\text{H}_2\text{O}}} \right)^{1/2}. \quad [4]$$

In Eq. [3], $D_{\text{H}_2, \text{H}_2\text{O}}$ and $D_{\text{H}_2, \text{k}}$ represent the binary and Knudsen diffusion coefficients, respectively, and they are given as:

$$D_{\text{H}_2, \text{H}_2\text{O}} = 0.018833 \sqrt{\frac{1}{M_{\text{H}_2}} + \frac{1}{M_{\text{H}_2\text{O}}}} \frac{T^{2/3}}{P \Omega_D \zeta_{\text{H}_2, \text{H}_2\text{O}}^2}, \quad [5]$$

$$D_{\text{H}_2, \text{k}} = \frac{2}{3} \left(\frac{8RT}{\pi M_{\text{H}_2}} \right)^{1/2} r. \quad [6]$$

The mean pore radius is assumed as $r = 0.75 \mu\text{m}$ in the present study, while Ω_D is the collision integral given as:

$$\Omega_D = 1.1336 \left(\frac{Tk}{\varepsilon} \right)^{-0.1814}. \quad [7]$$

TABLE I. Gas Properties.

Substance	M [g/mol]	ζ [Å]	ε/k [K]
H ₂	2.016	2.93	37
H ₂ O	18.015	2.65	356

TABLE II. Numerical Conditions.

Properties	Value
Operating temperature T [K]	1273
Total pressure p [Pa]	1.013×10^3
Fuel composition ($H_2:H_2O$) [mol%]	98.8:1.2
Electronic conductivity σ_{e^-} [Sm^{-1}] (11)	$3.27 \times 10^6 - 1065.3T$
Ionic conductivity $\sigma_{O^{2-}}$ [Sm^{-1}] (12)	$3.34 \times 10^4 \exp(-10300/T)$
Gibbs free energy ΔG° [J/mol]	-177.99×10^3

When calculating the binary diffusion coefficient, a intermolecular force constants ζ is taken as an arithmetic mean of ζ_{H_2} and ζ_{H_2O} . Geometric mean of ε_{H_2} and ε_{H_2O} is used for ε . The gas parameters are shown in Table I.

Assuming that Ni and YSZ are perfect electronic and ionic conductors, the following equations are solved in these phases:

$$\nabla \left(\frac{\sigma_{e^-}}{F} \nabla \tilde{\mu}_{e^-} \right) = -i_{\text{react}}, \quad [8]$$

$$\nabla \left(\frac{\sigma_{O^{2-}}}{2F} \nabla \tilde{\mu}_{O^{2-}} \right) = i_{\text{react}}, \quad [9]$$

where $\tilde{\mu}_{e^-}$ and $\tilde{\mu}_{O^{2-}}$ are the electrochemical potentials of electron and oxygen ion, respectively.

The reaction current i_{react} in the R.H.S. of Eqs. [3], [8] and [9], which is defined at TPB, is calculated from the Butler-Volmer equation (13) as:

$$i_{\text{react}} = i_0 L_{\text{TPB}} \left\{ \exp\left(\frac{2F}{RT} \eta_{\text{act}}\right) - \exp\left(-\frac{F}{RT} \eta_{\text{act}}\right) \right\}. \quad [10]$$

The lineal exchange current density i_0 is fitted from the patterned anode experiments of DeBoer *et al.* (14)

$$i_0 = 31.4 \times p_{H_2}^{-0.03} p_{H_2O}^{0.4} \exp\left(-\frac{1.52 \times 10^5}{RT}\right). \quad [11]$$

The numerical conditions in this study are listed in Table II.

Overpotential Calculation

From the LBM calculation, the electron electrochemical potential $\tilde{\mu}_{e^-}$ in the Ni phase, the oxygen ion electrochemical potential $\tilde{\mu}_{O^{2-}}$ in the YSZ phase and the oxygen chemical potential μ_o in the gaseous phase are obtained. The overpotential is defined as the voltage difference between the reference electrode (RE) and the working electrode (WE):

$$\eta = E_{\text{WE/S}} - E_{\text{RE/S}} = \frac{1}{F} \left(\tilde{\mu}_{e^-, \text{RE/S}} - \tilde{\mu}_{e^-, \text{WE/S}} \right), \quad [12]$$

where $\tilde{\mu}_{e^-,RE/S}$ and $\tilde{\mu}_{e^-,WE/S}$ are the electron electrochemical potentials at the surfaces of RE and WE, respectively. Local activation overpotential η_{act} at TPB is obtained by subtracting ohmic losses from the total overpotential. Figure 4 shows a schematic of the local activation overpotential, which is written as follows:

$$\begin{aligned} \eta_{act} &= \frac{1}{F}(\tilde{\mu}_{e^-,RE/S} - \tilde{\mu}_{e^-,WE/S}) - \frac{1}{F}(\tilde{\mu}_{e^-,RE/S} - \tilde{\mu}_{e^-,lyte/RE}) \\ &\quad - \frac{1}{F}(\tilde{\mu}_{e^-,lyte/WE} - \tilde{\mu}_{e^-,WE/S}) - \frac{1}{2F}(\tilde{\mu}_{O^{2-},lyte/RE} - \tilde{\mu}_{O^{2-},lyte/WE}) \quad . \quad [13] \\ &= -\frac{1}{2F} \left(2\tilde{\mu}_{e^-,lyte/WE} - \tilde{\mu}_{O^{2-},lyte/WE} + \left\{ \Delta G^\circ + RT \log \left(\frac{p_{H_2O}}{p_{H_2}} \right) \right\}_{RE} \right) \end{aligned}$$

In Eq. [13], the local equilibrium is assumed inside the electrolyte at the electrolyte/RE interface (15):

$$\tilde{\mu}_{O^{2-}} = 2\tilde{\mu}_{e^-} + \mu_O. \quad [14]$$

The total overpotential of anode η_{anode} is obtained by subtracting ohmic losses of current collector (CC), electrolyte and reference electrode with an assumption of the same gas composition at CC and RE as follows:

$$\begin{aligned} \eta_{anode} &= \frac{1}{F}(\tilde{\mu}_{e^-,RE/S} - \tilde{\mu}_{e^-,CC}) - \frac{1}{F}(\tilde{\mu}_{e^-,CC} - \tilde{\mu}_{e^-,anode/CC}) \\ &\quad - \frac{1}{2F}(\tilde{\mu}_{O^{2-},lyte/RE} - \tilde{\mu}_{O^{2-},anode/lyte}) - \frac{1}{F}(\tilde{\mu}_{e^-,RE/S} - \tilde{\mu}_{e^-,lyte/RE}) \quad . \quad [15] \\ &= -\frac{1}{2F} \left(2\tilde{\mu}_{e^-,anode/CC} - \tilde{\mu}_{O^{2-},anode/lyte} + \left\{ \Delta G^\circ + RT \log \left(\frac{p_{H_2O}}{p_{H_2}} \right) \right\}_{CC} \right) \end{aligned}$$

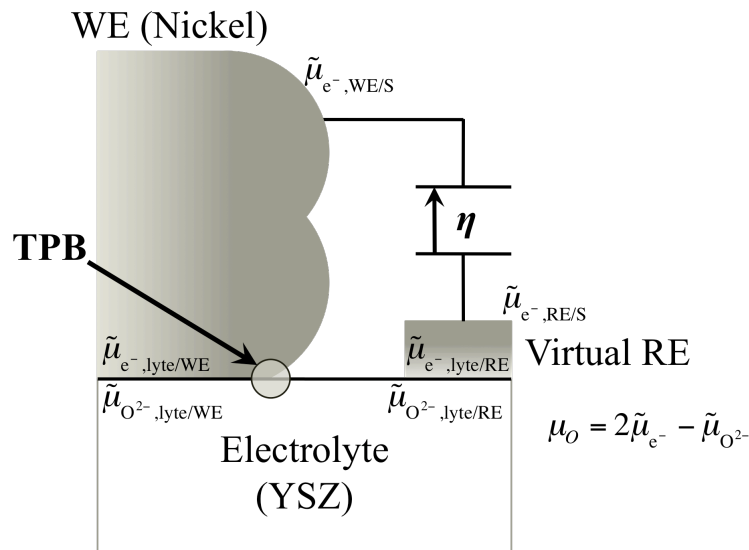


Figure 4. Schematic of local activation overpotential at TPB.

TABLE III. Total and connected TPB lengths.

Properties	Value
TPB length [m] (Total)	1.26×10^{-2}
TPB length [m] (Connected)	7.61×10^{-3}
TPB density [m/m^3] (Total)	2.58×10^{12}
TPB density [m/m^3] (Connected)	1.56×10^{12}

Three Phase Boundary Length

If neighboring four voxels are composed of three different phases, with diagonal voxel phases not being the same, the line segment surrounded by the four voxels is defined as a three phase boundary. Then, triangles are defined by the neighboring three midpoints of the three phase boundary segments. Finally, three phase boundary length is calculated as the distance between the centroids of these triangles (7). Table III shows the TPB length and density. In this table, a connected TPB is one of which the gaseous and Ni phases are connected to the current collector while at the YSZ phase to the electrolyte. The percentage of connected TPB is about 60 % of the total TPB length.

Computational Scheme

The LBM (8) is used to solve Eqs. [3], [8] and [9] in each phase. For the 3D LBM simulation, D3Q15 ($i = 1-15$) or D3Q19 ($i = 1-19$) models are commonly used. However, it has been shown that, in the case of simple diffusion simulation, D3Q6 ($i = 1-6$) model can be used with a slight loss of accuracy (16). So, the D3Q6 model is used in this study. The LB equation with the LBGK model in the collision term is written as follows:

$$f_i(\mathbf{x} + \mathbf{c}_i \Delta t, t + \Delta t) = f_i(\mathbf{x}, t) - \frac{1}{t^*} [f_i(\mathbf{x}, t) - f_i^{eq}(\mathbf{x}, t)] + w_i \Delta t. \quad [16]$$

In Eq. [16], f_i represents the density distribution function of gas, electron or ion with a velocity \mathbf{c}_i in the i -th direction, and f_i^{eq} is the Maxwellian local equilibrium distribution,

$$f_i^{eq}(\mathbf{x}, t) = \frac{1}{6} \sum_{i=1}^6 f_i(\mathbf{x}, t). \quad [17]$$

The relaxation time t^* is a function of diffusion coefficient D , voxel size Δx and time step Δt and it given as:

$$t^* = 0.5 + \frac{3D\Delta t}{\Delta x^2}. \quad [18]$$

In the present study, the time step Δt is chosen so that the relaxation time becomes $t^* = 0.99$. However, the DGM diffusion coefficient is not constant in the gaseous phase. So the relaxation time is changed according to the DGM diffusion coefficient. The last term of Eq. [16] is a production term calculated from the reaction current density i_{reac} . Adiabatic boundary condition is assumed at the boundaries of $x = 0, 8.43 \mu\text{m}$ and $y = 0, 6.2 \mu\text{m}$. At the current collector surface, constant gas composition (Dirichlet boundary) is applied. Constant electronic and ionic current flux conditions (Neumann boundary) are

imposed on the current collector and electrolyte boundaries, respectively. A no-flux boundary is imposed on the boundary of each phase in the porous media by applying the halfway bounceback scheme with a second-order accuracy (17).

Results

The predicted total overpotential η_{anode} is compared with the experimental data (9) in Figure 5. Current densities in LBM are changed as 0.01, 0.1, 0.3 and 0.7 [A/cm²]. As seen in this figure, the prediction agrees very well with the experimental data. However, it is reported that domain size of the present sample is not sufficiently large for calculating effective conductivities of Ni and YSZ phases (7). Thus, effect of computational domain size should be carefully investigated, which remains as a future task. The electrochemical potential distribution of oxygen ion in the YSZ phase is shown

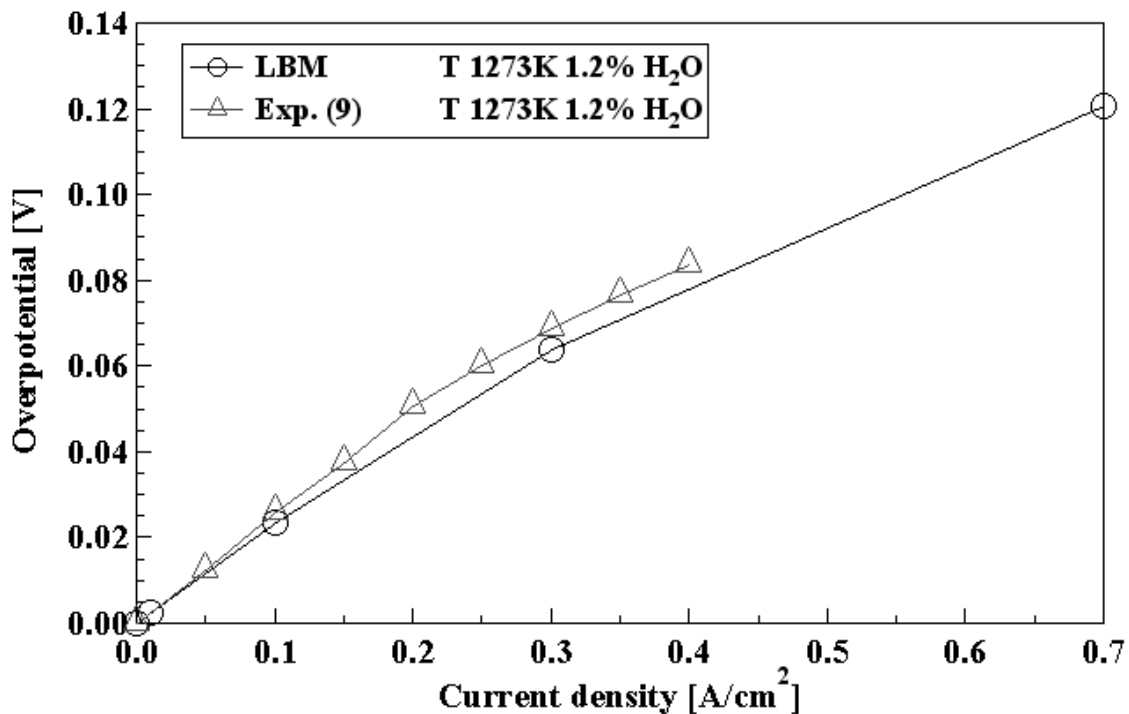


Figure 5. Comparison of predicted overpotential with the experimental data (9).



Figure 6. Distribution of oxygen ion electrochemical potential $\Delta\tilde{\mu}_{\text{O}^{2-}}$ in YSZ phase.

(a) $y = 4.34 \mu\text{m}$, (b) $z = 4.96 \mu\text{m}$.

in Figure 6. Figure 6(a) clearly shows the potential dropping from the electrolyte side to the current collector side. The potential distribution is not uniform in the x - y cross section as shown in Figure 6(b). This can be attributed to the non-uniform oxygen ion transport path through the YSZ phase, and also to the nonuniformity of distributed TPBs.

Conclusions

The anode overpotential and potential distributions in a three-dimensional microstructure reconstructed by FIB-SEM images are solved by using LBM. The predicted anode overpotential shows good agreement with the experimental data. The oxygen ion electrochemical potential distribution is not uniform in the x - y cross section. This can be attributed to the non-uniform oxygen ion transport path through the YSZ phase, and also to the nonuniformity of distributed TPBs.

Acknowledgments

This work was supported by the New Energy and Industrial Technology Development Organization (NEDO) under the Development of System and Elemental Technology of Solid Oxide Fuel Cell (SOFC) Project.

References

1. S. C. Singhal and K. Kendall, *High Temperature Solid Oxide Fuel Cells*, Elsevier (2002).
2. J. R. Wilson, W. Kobsiriphat, R. Mendoza, H.-Y. Chen, J.M. Hiller, D. J. Miller, K. Thornton, P.W. Voorhees, S. B. Adler and S. Barnett, *Nature Materials*, **5**, 541-544 (2006).
3. D. Gostovic, J. R. Smith, D. P. Kundinger, K. S. Jones and E. D. Wachsman, *Electrochemical and Solid-State Letters*, **10** (12), B214-B217 (2007).
4. J. R. Smith, A. Chen, D. Gostovic, D. Hickey, D. P. Kundinger, K. L. Duncan, R. T. DeHoff, K. S. Jones and E. D. Wachsman, *Solid State Ionics*, **180**, 90-98 (2009).
5. J. R. Wilson, M. Gameiro, K. Mischaikow, W. Kalies, P. Voorhees and S. Barnett, *Microsc. Microanal.*, **15**, 71-77 (2009).
6. J. R. Izzo, Jr., A. S. Joshi, K. N. Grew, W. K. S. Chiu, A. Tkachuk, S. H. Wang and W. Yun, *J. Electrochem. Soc.*, **155** (5), B504-B508 (2008).
7. H. Iwai *et al.*, SOFC XI, to be presented (2009).
8. Y. Suzue, N. Shikazono and N. Kasagi, *J. Power Sources*, **184**, 52-59 (2008).
9. T. Matsui *et al.*, SOFC XI, to be presented (2009).
10. R. Krishna and J. A. Wesselingh, *Chem. Eng. Sci.*, **52**, 861-911 (1997).
11. U. Anselmi-Tamburini, G. Chiodelli, M. Arimondi, F. Maglia, G. Spinolo and Z. A. Munir, *Solid State Ionics*, **110**, 35-43 (1998).
12. J. R. Ferguson, J. M. Flard and R. Herbin, *J. Power Sources*, **58**, 109-122 (1996).
13. T. Kawada, N. Sakai, H. Yokokawa and M. Dokiya, *J. Electrochem. Soc.*, **137**, 3042-3047 (1990).
14. B. DeBoer, *Ph.D. Thesis, University of Twente, The Netherland* (1998).
15. J. Mizusaki, K. Amano, S. Yamauchi and K. Fueki, *Solid State Ionics*, **22**, 313-322 (1987).

16. T. H. Zeiser, P. Lammers, E. Klemm, Y. W. Li, J. Bernsdorf and G. Brenner, *Chem. Eng. Sci.*, **56**, 1697-1704 (2001).
17. M. A. Gallivan, D. R. Noble, J. G. Georgiadis and R. O. Buckius, *Int. J. Numer. Methods Fluids*, **25**, 249-263 (1997).